

Thermonuclear Reaction Rate of $3\text{He}(\alpha;\gamma)7\text{Be}$ Process

Maryam Khoddam (✉ khoddam.nm1@gmail.com)

Arak University

Hossein Sadeghi

Arak University

Shahla Nahidinezhad

Arak University

Research Article

Keywords: Reaction Rate, Radiative Capture, Effective Field Theory, Astrophysical Energies

Posted Date: April 20th, 2022

DOI: <https://doi.org/10.21203/rs.3.rs-1561290/v1>

License: © ⓘ This work is licensed under a Creative Commons Attribution 4.0 International License.

[Read Full License](#)

Thermonuclear Reaction Rate of ${}^3\text{He}(\alpha, \gamma){}^7\text{Be}$ Process

M. Khoddam, H. Sadeghi, S.Nahidinezhad

Abstract The reaction rate of ${}^3\text{He} - \alpha$ radiation capture process has been calculated in astrophysical energies using the pionless Effective Field Theory(EFT) using the Faddeev equation approach up to Next-to Leading Order(NLO) while taking Coulomb interaction into account. The findings for the E_1 and E_2 transitions to the ${}^7\text{Be}$ ground state have been normalized using NACRE 1999 experimental data and compared to certain theoretical and experimental data.

Keywords Reaction Rate; Radiative Capture; Effective Field Theory; Astrophysical Energies

1 Introduction

The Big Bang nucleosynthesis (BBN) is defined in physical cosmology as the collection of fundamental nuclear interactions that produced nuclei other than the lightest hydrogen isotope during the early phases of Universe development. Nuclei such as ${}^7\text{Be}$ are involved in the early stages of the synthesis of other nuclei such as ${}^7\text{Li}$. Because the thermonuclear reaction rate of the ${}^3\text{He}(\alpha, \gamma){}^7\text{Be}$ is dependent on ${}^7\text{Li}$ generation in BBN, measuring or computing the observables of this reaction in astronomical energies can be useful in solving the following challenges. To predict reaction processes and how to release the energy in nuclear interactions, it is generally required to know the rate of interactions. Many astrophysical simulations also need a comprehensive understanding of reaction rates. Of course, in many cases, the rate of reactions cannot be directly measured, so indirect nuclear techniques have been applied.

Several experimental investigations have been made to identify several variables related to the ${}^3\text{He}(\alpha, \gamma){}^7\text{Be}$ reaction, such as cross-section, astrophysical factor, and reaction rate, using various approaches. Angulo, C. et al. (1999) obtained cross-section and reaction rate data for 86 charged-particle driven reactions in low energies. Nara Singh, B. S. et al. (2004), Confortola, F. et al. (2007), Brown, T. A. D. et al. (2007), Di Leva, A. et al. (2009), and many others have studied different characteristics of the ${}^3\text{He}(\alpha, \gamma){}^7\text{Be}$ reaction utilizing various techniques such as activation and prompt gamma rays. The work of Angulo, C. et al. (1999) for nuclei with the mass number $A < 16$ has been presented by Xua, Y. et al. (2013) and Kontos, A. et al. (2013) have also used prompt gamma-ray detection from the ${}^3\text{He}(\alpha, \gamma){}^7\text{Be}$ reaction in the energy range of 300- 1460 keV and has performed the R-matrix analysis using capture reaction data to determine the reaction rate. Takacs, M.P. et al. (2015) used the solar model and flux of neutrinos to determine the ${}^3\text{He}(\alpha, \gamma){}^7\text{Be}$ astrophysical S-factor at the solar Gamow peak, and by re-evaluating the S-factor. They also determined the thermonuclear reaction rate at BBN energy.

Different procedures have been used in the theoretical field to determine the ${}^3\text{He}(\alpha, \gamma){}^7\text{Be}$ reaction rate and other physical observables of this procedure, such as the Monte Carlo method by Nollett, K.M. et al. (2000), using highly accurate experimental data technique and examining the ${}^3\text{He}(\alpha, \gamma){}^7\text{Be}$ data to find the reaction rate, and estimating the primordial abundance of ${}^7\text{Li}$ and $S_{34}(0)$ by Cyburt, R. H. et al. (2008), Canton, L. et al. (2008), Neff, T. (2010), and Neff, T. (2011) used the microscopic many-body procedure along with the fermionic molecular dynamics method (FMD) and the AV18 potential to calculate cross-section and S-factor at low energies. deBoer, R. J. et al. (2014) have used R-matrix fit to represent the ${}^3\text{He}(\alpha, \gamma){}^7\text{Be}$ data, whereas Sadeghi, H. et al. (2013, 2018) estimated the observ-

M. Khoddam, H. Sadeghi, S.Nahidinezhad

Department of Physics, Faculty of Science, Arak University, Arak 8349-8-38156, Iran.

e-mail: khoddam.nm1@gmail.com

able of this reaction using the M3Y and local two-body nucleon-nucleon potentials at low energies. Iliadis, C. et al. (2016) reported the S-factor and reaction rate employing Bayesian statistics, and Tursunov, E.M. et al. (2019) recently used a two-body potential model to estimate the reaction rate as well as the abundance of ${}^7\text{Li}$.

In this work, we calculated the reaction rate of ${}^3\text{He}(\alpha, \gamma){}^7\text{Be}$ in the Effective Field Theory(EFT) framework and using the Faddeev equations method in LO and NLO considering the Coulomb corrections using our recent computational data for the cross-section of E_1 and E_2 transitions to the ground state, Khoddam. M. et al. (2022a). Pionless EFT is also used in systems with few nucleons where the momentum is less than the pion's mass ($Q \ll m_\pi$). Over the last few decades, EFT has been used in a variety of investigations. Sadeghi, H. et al, (2013); Sadeghi, H. et al. (2014a,b) investigated proton-deuteron radiative capture at LO, neutron-deuteron reaction up to N²LO, and ${}^2\text{H}(d, \gamma){}^4\text{He}$ reaction. Zhang, X. et al. (2020) also used the EFT at NLO to extrapolate data. Premarathna et al. investigated a comparison of two conflicting EFT power counting models at low energies. Furthermore, Higa, R. et al. (2018) employed halo EFT to determine the E_1 transition of the ${}^3\text{He}(\alpha, \gamma){}^7\text{Be}$ reaction. Recent studies in EFT, is the calculation of cross-section, S-factor, and thermonuclear reaction rate, for $d(\alpha, \gamma){}^6\text{Li}$ reaction up to NLO, by Nahidinezhad, S. et al. (2020a,b, 2021, 2022). Because an alpha particle with a boundary energy of 20 MeV will not be excited in the low energy range, it has been thought to be the structureless particle. ${}^3\text{He}$ has also thought of it as a two-body (pd). With these assumptions, the scattering amplitude, cross-section, and S-factor for this interaction in the E_1 and E_2 electrical transitions from the initial states of $2s_{1/2}$, $2p_{1/2}$, and $3s_1$ to the final state of $2p_{3/2}$ in ${}^7\text{Be}$ have been calculated up to LO without Coulomb corrections and up to NLO with Coulomb considerations.

Section 2 of this paper briefly describes the theoretical computational model following the incorporation of effective Lagrangian and Faddeev integral equations, and Section 3 presents the findings of the reaction rate calculation, as well as the accompanying graphs and tables. The final section includes a summary and conclusion.

2 Theoretical Method

The formulation of a pionless EFT was employed in this work. As explained in our last works, we assumed

${}^3\text{He}$ as a two-body structure consisting of deuteron and proton, and an alpha particle with no internal structure. We have considered three processes to calculate the scattering amplitude and cross-section of the ${}^3\text{He}(\alpha, \gamma){}^7\text{Be}$ reaction: elastic scattering (α, pd), proton exchange ($d, p\alpha$), and deuteron exchange channel ($p, d\alpha$). There are a spectator and an interactive pair in each channel. According to the selection roles permitted transitions for every channel have recognized, and the electrical transitions of E_1 and E_2 from the initial states of $2S_{1/2}$, $1P_{1/2}$ and $3S_1$ to the final ground state of $2P_{3/2}$ in ${}^7\text{Be}$ have chosen to calculate. Based on these interaction channels, the effective Lagrangian of the system has defined as the sum of one-body, two-body, and Coulomb interaction sentences, as follows,

$$\mathcal{L} = \mathcal{L}_{1b} + \mathcal{L}_{2b} + \mathcal{L}_{(ph)}. \quad (1)$$

The first part of the Lagrangian is the one-body section, the second part is the two-body section up to NLO, and the third one is related to the photon interaction up to NLO.

$$\begin{aligned} \mathcal{L}_{1b} &= N^\dagger (i\partial_0 + \frac{\nabla^2}{2M_N}) N + \phi_\alpha^\dagger (i\partial_0 + \frac{\nabla^2}{2M_\alpha}) \phi_\alpha \\ &+ d_s^\dagger (i\partial_0 + \frac{\nabla^2}{2M_d}) d_s \end{aligned} \quad (2)$$

$$\begin{aligned} \mathcal{L}_{2b} &= \sum_{n=0}^3 C_n^{(0)} T_i^\dagger \left[i\partial_0 + \frac{\nabla^2}{2(M_\alpha + \mu_{d\alpha})} - \Delta_0^{(0)} \right]^n T_i \\ &+ \sum_{n=0}^3 C_n^{(1)} T_i^\dagger \left[i\partial_0 + \frac{\nabla^2}{2(M_p + \mu_{d\alpha})} - \Delta_1^{(1)} \right]^n T_i \\ &+ \sum_{n=0}^3 C_n^{(0)} T_i^\dagger \left[i\partial_0 + \frac{\nabla^2}{2(M_d + \mu_{p\alpha})} - \Delta_2^{(0)} \right]^n T_i \\ &+ g_0^{(0)} \left[T_i^\dagger (\phi_\alpha \mathcal{O}_0^{(0)}(Nd_s)) + (\phi_\alpha \mathcal{O}_0^{(0)}(Nd_s))^\dagger T_i \right] \\ &+ g_1^{(1)} \left[T_i^\dagger (N\mathcal{O}_1^{(1)}(d_s\phi_\alpha)) + (N\mathcal{O}_1^{(1)}(d_s\phi_\alpha))^\dagger T_i \right] \\ &+ g_2^{(0)} \left[T_i^\dagger (d_s\mathcal{O}_2^{(0)}(N\phi_\alpha)) + (d_s\mathcal{O}_2^{(0)}(N\phi_\alpha))^\dagger T_i \right] \\ &+ g_0^{(0)} \left[\Psi_{(\tau Be)}^\dagger (\phi_\alpha(Nd_s)) + (\phi_\alpha(Nd_s))^\dagger \Psi_{(\tau Be)} \right] \\ &+ g_1^{(1)} \left[\Psi_{(\tau Be)}^\dagger (N(d_s\phi_\alpha)) + (N(d_s\phi_\alpha))^\dagger \Psi_{(\tau Be)} \right] \\ &+ g_2^{(0)} \left[\Psi_{(\tau Be)}^\dagger (d_s(N\phi_\alpha)) + (d_s(N\phi_\alpha))^\dagger \Psi_{(\tau Be)} \right] \\ &- h \left[(\mathcal{O}\Psi_{(\tau Be)})^\dagger T_i + h.c. \right] + \dots, \end{aligned} \quad (3)$$

where N (M_N), ϕ_α (M_α) and d_s ($M_d = 2M_N$) are the field (mass) of the nucleon, alpha, and deuteron, respectively. The intermediate state composite array of ${}^7\text{Be}$ (consisting of alpha and ${}^3\text{He}$) is denoted by T_i , and the field of ${}^7\text{Be}$ in the ground state is showed by $\Psi_{(\tau Be)}$. Here the dimeron field of nucleon and deuteron in the

s -wave initial state, nucleon and alpha in the p -wave initial state, and the dimeron field of deuteron and alpha in the s -wave initial state are presented by (Nd_s) , $(N\phi_\alpha)$ and $(d_s\phi_\alpha)$, respectively. $C_n^{(l)}$, ($n = 0 - 3$) is the elastic scattering coupling constant obtained in ($l = 0, 1$) using the RMS parameter. $g_i^{(l)}$ is the coupling constant obtained phenomenologically for the transition from dimeron fields to the intermediate states, $g_i^{(l)} = \sqrt{6\pi\mu}$, ($i = 0 - 2$), ($l = 0, 1$) is the coupling constant, and μ shows the reduced mass of alpha and 3He . h is the renormalization constant and \mathcal{O} is a dimeron-to-final-state transition operator for ($l = 0, 1$) channels defined as follows,

$$\mathcal{O} = \left(\frac{\vec{D}}{M_i} - \frac{\overleftarrow{D}}{M_j} \right). \quad (4)$$

The third part of Lagrangian is related to the photon interaction. The photonic components must be entered in calculations using the minimal substitution in addition to the strong interaction, up to NLO.

$$\begin{aligned} \mathcal{L}_{ph} &= \frac{N^\dagger N e Q_{({}^3He)}}{2m_{({}^3He)}} [\vec{p}_{({}^3He)} + \vec{p}'_{({}^3He)}] \vec{e}_\gamma^* \\ &+ \frac{N^\dagger N e Q_\alpha}{2m_\alpha} [\vec{p}_\alpha + \vec{p}'_\alpha] \vec{e}_\gamma^* \\ &- L_E^{({}^3He)} \Sigma_i \psi_{({}^3He)_i}^\dagger (\nabla^2 A_0 - \partial_0(\nabla \cdot A)) \psi_{({}^3He)_i} \\ &- L_E^{(N\alpha)} \Sigma_i (N\phi_\alpha)_i^\dagger (\nabla^2 A_0 - \partial_0(\nabla \cdot A)) (N\phi_\alpha)_i \\ &- L_E^{(d_s\alpha)} \Sigma_i (d_s\phi_\alpha)_i^\dagger (\nabla^2 A_0 - \partial_0(\nabla \cdot A)) (d_s\phi_\alpha)_i, \end{aligned} \quad (5)$$

where \vec{e}_γ^* is the photon's polarization. The charge of α and 3He with the \vec{p} and \vec{p}' momentum, are represented with $Q_\alpha = 2$ and $Q_{({}^3He)} = 2$ respectively. And L_{E_1} , L_{E_2} and L_{E_3} are the unknown phenomenological coupling constants at NLO for 3He , (p, α) and (d, α) into real photons, which are found phenomenologically to be $L_E^{({}^3He)} = L_E^{(N\alpha)} = L_E^{(d_s\alpha)} = 0.034$. The first two lines of Eq. (5) are related to the leading order and the three last lines are the NLO order of interaction. The diagrams describing the photon part of radiative capture of ${}^3He - \alpha$ reaction are presented in Fig. 4. We briefly introduce the Faddeev computational method. According to Ji, C. et al. (2014), the Faddeev equation can be written for every spectator in each channel as follow,

$$\begin{aligned} \mathcal{F}_i(q) &= \sum_{j \neq i} 4\pi \int_0^\Lambda q'^2 dq' \mathcal{X}_{ij}(q, q';) \\ &\times \tau_j(q'; E) \mathcal{F}_j(q'), \end{aligned} \quad (6)$$

where λ is the ultraviolet cut off ($\lambda = m_\pi$), \mathcal{X}_{ij} and τ_j are the kernel functions and two-body matrices respectively with the following definitions,

$$\begin{aligned} \mathcal{X}_{ij}(q, q'; E) &= \iint p^2 dp p'^2 dp' g_{l_i}(p) \mathcal{G}_0^{(i)}(p, q; E) \\ &\times g_{l_j}(p') \quad i < p, q; \Omega_i \mid p', q'; \Omega_j >_j, \end{aligned} \quad (7)$$

$$\begin{aligned} \tau_i(q; E) &= \tau_{jk} \left(E - \frac{q^2}{2\mu_{i(jk)}} \right) \\ \tau_{ij}(E) &= \frac{1}{4\pi^2 \mu_{ij} (\gamma_0 + ik)}, \quad k = \sqrt{2\mu_{ij} E}, \end{aligned} \quad (8)$$

where the subscripts i and j describe the spectator and exchanged particle, respectively. The three-body Green function, $\mathcal{G}_0^{(i)}(p, q; E)$ is given by

$$\mathcal{G}_0^{(i)}(p, q, E) = \left(E - \frac{p^2}{2\mu_{ij}} - \frac{q^2}{2\mu_{i(jk)}} \right)^{-1}. \quad (9)$$

The two-body form factors are denoted by $g_{l_i}(p)$ and $g_{l_j}(p')$. The free Hamiltonian eigenstate projection $i < p, q; \Omega_i \mid p', q'; \Omega_j >_j$, projects the free eigenstate in the observer's partition i onto the free eigenstate in the viewer's partition j . We have calculated it for the different viewers on every channel. For each spectator i in the three-body system, the eigenstates have been generally characterized. After determining the quantum numbers of the spin, angular momentum, and total angular momentum in each channel, we may write them for the 7Be system

$$\mid p, q; \Omega_i >_i = \sum_{L_i, S_i} \sqrt{\hat{J}_i \hat{I}_i \hat{L}_i \hat{S}_i} \begin{Bmatrix} l_i & s_i & j_i \\ \lambda_i & \sigma_i & I_i \\ L_i & S_i & J \end{Bmatrix} \times$$

$$\mid p, q; (l_i, \lambda_i) L_i; ((\nu_j, \nu_k) s_i, \sigma_i) S_i; J = M_j >_i, \quad (10)$$

The orbital and spin angular momentum of the pair/viewer is denoted by l/λ and s/σ , respectively, and the sum of them is denoted by L and S . The parameters ν_j, ν_k are the spins of each of the pair components (j, k). The orbital and spin components should then be separated using the following equation;

$$\begin{aligned} \mid p, q; \Omega_i >_i &= \sum_{M_L} \sum_{M_S} \mathcal{C}(L, S, J \mid M_L, M_S, M_J) \\ &\times \mid p, q; (l_i, \lambda_i); L_i, M_{L_i} > \\ &\times \mid [(\nu_j, \nu_k) s_i, \sigma_i] S_i, M_{S_i} >, \end{aligned} \quad (11)$$

where Clebsch-Gordan coefficients are defined as follows,

$$\mathcal{C}(L, S, J \mid M_L, M_S, M_J) =$$

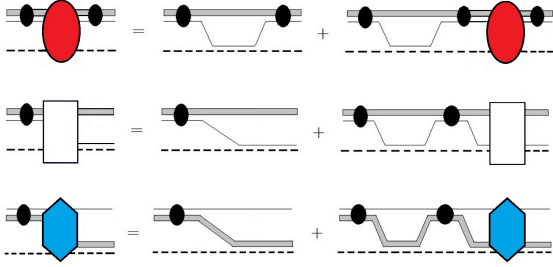


Fig. 1 The leading order Feynman diagrams associated to the scattering state without Coulomb effects and proton and deuteron exchange. The solid line, double filled line, and dashed line represent nucleon, deuteron, and alpha propagators, respectively. The amplitudes of ${}^3\text{He} - \alpha$ scattering state are represented by ovals, whereas the amplitudes in the proton and deuteron transfer channels are defined by rectangulars and hexagonals, respectively.

$$(-1)^{L-S+M_J} \sqrt{2j+1} \begin{Bmatrix} L & S & J \\ M_L & M_S & -M_J \end{Bmatrix}. \quad (12)$$

The matrix elements of the spin parts for different observers are given

$$\begin{aligned} & \langle s_1, (s_2, s_3) s_{23}; S | (s_1, s_2) s_{12}, s_3; S \rangle = \\ & (-1)^{s_1+s_2+s_3+S} \sqrt{(2s_{12}+1)(2s_{23}+1)} \\ & \times \begin{Bmatrix} s_1 & s_2 & s_{12} \\ s_3 & S & s_{23} \end{Bmatrix}. \end{aligned} \quad (13)$$

The inside of the brackets indicates the Wigner symbol $(6-j)$. The corresponding eigenstates to construct the general matrix elements for each spectator's orbital component in each channel are given by

$${}_i^n \langle p, q, (l_i, \lambda_i), L_i, M_{L_i} | p', q', (l_j, \lambda_j), L_j, M_{L_j} \rangle_j^m, \quad (14)$$

where the spectator's n_{th} and m_{th} eigenstates represent n and m , respectively. To compute kernel functions, we must first sum the matrix elements of (16) obtained for the same i and j , then substitute in Eq. (7). We next create the new function of $\mathcal{Z}_{ij}(q, q'; E)$ as a common component of the kernel function (see Khoddam, M. et al. (2022a), for more details);

$$\begin{aligned} \mathcal{Z}_{ij}(q, q'; E) &= \iint p^2 dp p'^2 dp' g_{l_i}(p) \mathcal{G}_0^{(i)}(p, q; E) \\ &\times g_{l_j}(p') {}_i \langle p, q; \Omega_i | p', q'; \Omega_j \rangle_j. \end{aligned} \quad (15)$$

We can rewrite the Faddeev equation in Eq. (6) for different spectators as

$$\begin{aligned} \mathcal{F}_\alpha(q) &= 4\pi \int_0^\Lambda q'^2 dq' \mathcal{X}_{\alpha p}(q, q'; E) \tau_p(q'; E) \mathcal{F}_p(q') \\ &+ 4\pi \int_0^\Lambda q'^2 dq' \mathcal{X}_{\alpha d}(q, q'; E) \tau_d(q'; E) \mathcal{F}_d(q'), \\ \mathcal{F}_p(q) &= 4\pi \int_0^\Lambda q'^2 dq' \mathcal{X}_{p\alpha}(q, q'; E) \tau_\alpha(q'; E) \mathcal{F}_\alpha(q') \\ &+ 4\pi \int_0^\Lambda q'^2 dq' \mathcal{X}_{pd}(q, q'; E) \tau_d(q'; E) \mathcal{F}_d(q'), \\ \mathcal{F}_d(q) &= 4\pi \int_0^\Lambda q'^2 dq' \mathcal{X}_{d\alpha}(q, q'; E) \tau_\alpha(q'; E) \mathcal{F}_\alpha(q') \\ &+ 4\pi \int_0^\Lambda q'^2 dq' \mathcal{X}_{dp}(q, q'; E) \tau_p(q'; E) \mathcal{F}_p(q'). \end{aligned} \quad (16)$$

Figure 1 depicts diagrams relating to these equations that do not include the Coulomb corrections. To compute the Faddeev equations in NLO, the relations $\mathcal{F}_\alpha(q')$, $\mathcal{F}_p(q')$ and $\mathcal{F}_d(q')$ must be substituted in the leading order's Faddeev equations to obtain three one-channel integral equations that are simply in terms of one Faddeev equation. As shown below, Faddeev equations and kernel functions up to NLO may be generated

$$\begin{aligned} \mathcal{F}_i(q) &= 4\pi \int_0^\Lambda q'^2 dq' \mathcal{D} [4\pi \int_0^\Lambda q''^2 dq'' \chi'_{ij}(q, q''; E) \\ &\times \tau_j(q''; E) \chi'_{ji}(q'', q'; E)] \tau_i(q'; E) \\ &+ 4\pi \int_0^\Lambda q'^2 dq' \mathcal{D} [4\pi \int_0^\Lambda q''^2 dq'' \chi'_{jk}(q, q''; E) \\ &\times \tau_k(q''; E) \chi'_{kj}(q'', q'; E)] \tau_i(q'; E) \\ &+ 4\pi \int_0^\Lambda q'^2 dq' \mathcal{D} [4\pi \int_0^\Lambda q''^2 dq'' \chi'_{ki}(q, q''; E) \\ &\times \tau_i(q''; E) \chi'_{ik}(q'', q'; E)] \tau_j(q'; E), \end{aligned} \quad (17)$$

$$\begin{aligned} \chi'_{ij}(q, q'; E) &= \iint p^2 dp p'^2 dp' g_{l_i}(p) \mathcal{G}_0^{(i)}(p, q; E) L_E^{(ij)} \\ &\times g_{l_j}(p') {}_i \langle p, q; \Omega_i | p', q'; \Omega_j \rangle_j, \end{aligned} \quad (18)$$

where $E = -B_3$ and $\mu_{i(jk)}$ are the three-body binding energy and reduced mass, respectively. $\mathcal{D} = \mathcal{D}_{s(pp)}$ is the i_{th} spectator's two-proton propagator for the pp interaction

$$\begin{aligned} i\mathcal{D}_{s(pp)}(E - \frac{3q^2}{4M_p}) &= \frac{4\pi}{M_p g_s^2} \frac{-i}{-\frac{4\pi\Delta_s^R}{M_p g_s^2} - 2K\mathcal{H}(K/p')}, \\ \mathcal{H}(\eta) &= \psi(i\eta) + \frac{1}{2i\eta} - \ln(i\eta), \end{aligned} \quad (19)$$

where $\psi(i\eta)$ represents gamma function's logarithmic derivative, and Δ_s^R is renormalization constant.

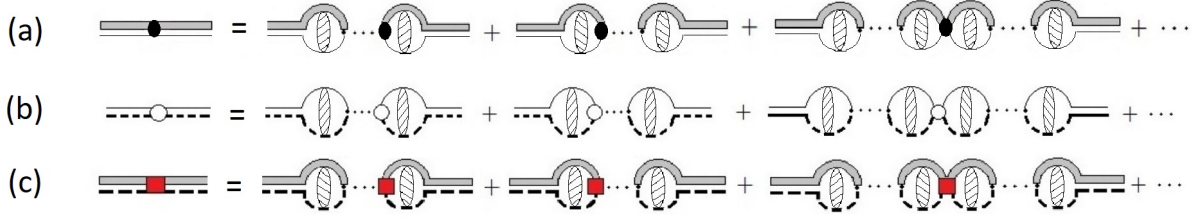


Fig. 2 Definitions of (a) proton-deuteron (b) proton-alpha (c) deuteron-alpha propagators involved in Coulomb interactions up to NLO. The NLO vertices (p and d), (p and α), and (d and α) are represented as black ovals, open circles, and squares, respectively.

Numerical calculations of the Faddeev equation have been completely discussed in Khoddam. M. et al. (2022a). The transition amplitudes can be written as,

$$\left| E_l^{L,S,J_i,J_f} \right|^2 = \left(\frac{1}{3} \mathcal{F}_\alpha \right)^2 + \left(\frac{1}{3} \mathcal{F}_p \right)^2 + \left(\frac{1}{3} \mathcal{F}_d \right)^2. \quad (20)$$

The following equation shows the radiation capture cross-section at low energy,

$$\sigma = \frac{1}{f} \frac{q}{1 + \frac{q}{\mu}} \Sigma_{L,S,J_i,J_f} \frac{1}{2J_f + 1} \left| E_l^{L,S,J_i,J_f} \right|^2, \quad (21)$$

$f = \frac{v_{rel}}{8\pi\alpha}$, where v_{rel} is the relative velocity of 3He and alpha.

Figure 3 shows Feynman diagrams of the amplitude associated with elastic scattering channels, proton, and deuteron transfer in NLO, which are all involved in Coulomb effects. Figures 3(a), 3(b), and 3(c) illustrate the perturbative expansion of proton-deuteron, proton-alpha, and deuteron-alpha propagators, including Coulomb interactions up to NLO.

The number of thermonuclear reactions performed in one cubic centimeter per second is referred to as the thermonuclear reaction rate. This is determined by the relative velocities of the initial particles, the numerical density of the reactants (a,b), and the interaction cross-section

$$r_{ab} = \frac{N_a N_b \sigma(v) v}{1 + \delta_{ab}}, \quad (22)$$

where the Kronecker delta, δ_{ab} , is utilized since the same interaction pairings are not counted again. The cross-section is a function of the particle's velocity due to the electrostatic repulsion of the reactants (as well as atomic resonances). As a result, determining the velocity of the reactions by measuring their cross-section at different energies is the most reliable method. To compute the reaction velocity in interstellar nuclear interactions, such as the radiation capture process, one

must integrate over a velocity distribution in the form of a Maxwell-Boltzmann distribution. The range of energies at which the integral must be considered in determining the reaction rate. The Gamow window is a term that refers to this range of energy. Thus

$$r_{ab} = (1 + \delta_{ab})^{-1} N_a N_b \int_0^\infty \sigma(v) v \phi(v) dv, \quad (23)$$

where $\phi(v)$ is the Maxwell-Boltzmann distribution function, which is defined in the center of mass frame as follows,

$$\phi(v) dv = 4\pi v^2 \left(\frac{\mu}{2\pi k_B T} \right)^{3/2} \exp\left(\frac{-\mu v^2}{2k_B T} \right) dv, \quad (24)$$

where k_B denotes the Boltzmann's constant, T the temperature in Kelvin, and $\mu = \frac{M_a M_b}{M_a + M_b}$ the reduced mass of the interacting particles. The thermonuclear reaction rate is given by,

$$\begin{aligned} N_A \langle \sigma v \rangle &= N_A 4\pi \left(\frac{\mu}{2\pi k_B T} \right)^{3/2} \int_0^\infty v^3 \sigma(v) \\ &\times \exp\left(\frac{-\mu v^2}{2k_B T} \right) dv \\ &= N_A \left(\frac{8}{\pi\mu} \right)^{1/2} \left(\frac{1}{k_B T} \right)^{3/2} \\ &\times \int_0^\infty \sigma(E) E \exp\left(\frac{-E}{k_B T} \right) dE \end{aligned} \quad (25)$$

If the variable $k_B T$ is expressed in units of MeV, $\langle \sigma v \rangle$ would be in units of ($cm^3 mol^{-1} s^{-1}$). In this case, it is more appropriate to use the variable T_9 for the temperature with a unit of 10^9 Kelvin. After substituting the constant values in the expression above, the reaction rate is expressed as follows,

$$\begin{aligned} N_A \langle \sigma v \rangle &= 3.7313 \times 10^{10} A^{-1/2} T_9^{-3/2} \\ &\times \int_0^\infty \sigma(E) E \exp\left(-11.605 \frac{E}{T_9} \right) dE \end{aligned} \quad (26)$$

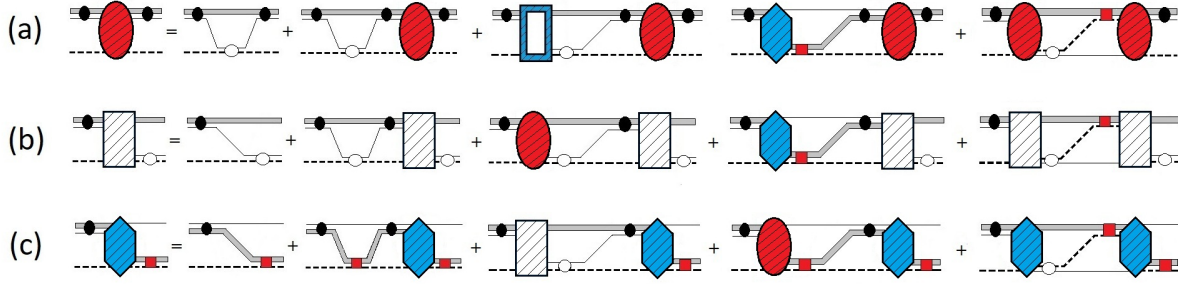


Fig. 3 Diagrams demonstrating the Faddeev integral equation of the two-body elastic scattering channels. ovals represent ${}^3\text{He} - \alpha$ elastic scattering. The kernels of ${}^3\text{He}$ and α scattering in the proton and deuteron exchange channels are shown by rectangles and hexagonal symbols, respectively. The remaining notations are the same as in last figures.

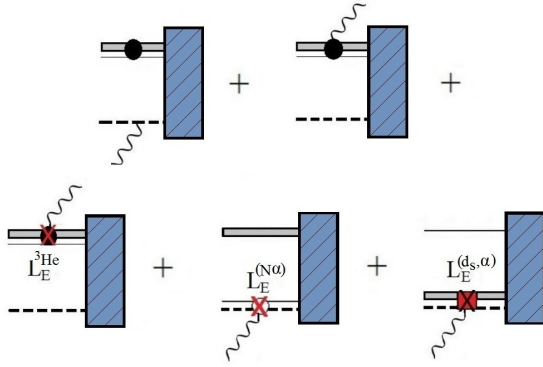


Fig. 4 Diagrams showing the photon capture process in the ${}^3\text{He} - \alpha$ radiative capture reaction. The solid line, double filled line, and dashed line represent the nucleon, deuteron, and alpha propagators respectively. Real photons are depicted by the wavy lines. And the $(p$ and $d)$, $(p$ and $\alpha)$, and $(d$ and $\alpha)$ NLO vertices are represented as black ovals, open circles, and squares, respectively. And the black rectangular describes the intermediate composite array of ${}^7\text{Be}$.

3 Result and discussion

The ${}^3\text{He}(\alpha, \gamma){}^7\text{Be}$ thermonuclear reaction rate was computed in this work using our computational results, Khoddam. M. et al. (2022a,b) for the cross-section in astrophysical energies using EFT formalism and by means of Faddeev equation technique up to NLO, with the following assumptions: We defined ${}^3\text{He}$ as a two-body structure composed of proton and deuteron with masses of $M_p = 938$ MeV and $M_d = 1876$ MeV. Alpha particles with binding energies of $E_\alpha = 20$ MeV were considered structureless because they cannot be excited in the low-energy region. Three possible channel was considered for the ${}^3\text{He} - \alpha$ scattering process, (α, pd) , $(d, p\alpha)$, and $(p, d\alpha)$, which are correspond to the elastic scattering ${}^3\text{He} + \alpha \rightarrow {}^3\text{He} + \alpha$, the proton transfer ${}^3\text{He} + \alpha \rightarrow d + p\alpha$, and the deuteron transfer

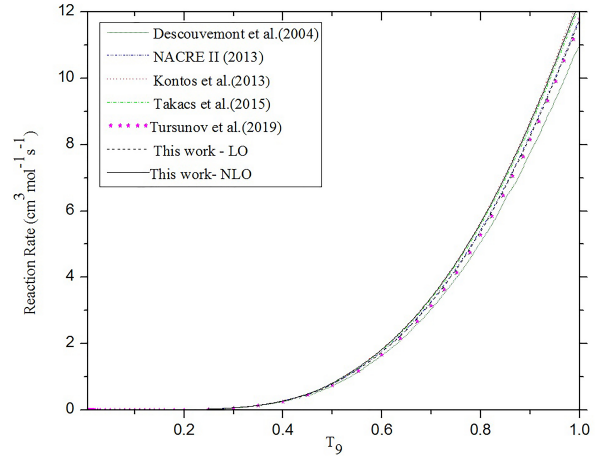


Fig. 5 The thermonuclear reaction rate of ${}^3\text{He}(\alpha, \gamma){}^7\text{Be}$ in the $10^6 K \leq T \leq 10^9 K$ ($0.001 \leq T_9 \leq 1$) temperature range in LO (dashed line) and NLO (solid line), as compared to other theoretical and experimental data.

${}^3\text{He} + \alpha \rightarrow p + d + \alpha$ processes, respectively (see Khoddam. M. et al. (2022a,b), for more details). The possible transitions in each channel are determined by the sum of the orbital and spin angular momenta, according to the selection rules. For the three defined processes, the transitions (E_1, M_2) and (E_2, M_1) are known as dominant transitions, and the electrical ones, E_1 and E_2 from $2s_{1/2}$, $2p_{1/2}$, and $3s_1$ to the $2p_{3/2}$ ground state in ${}^7\text{Be}$ have been chosen to study, with the E_1 transition being the predominant. Since we used the Faddeev equation approach, the three Faddeev equations for the three spectators corresponding to three processes were computed after solving the kernel functions in LO and NLO with Coulomb interactions, and the cross-section was calculated for $E \leq 1.5$ MeV.

The numerical computations are fully discussed in the Khoddam. M. et al. (2022a) publication. We utilized the findings of prior computations to calculate the

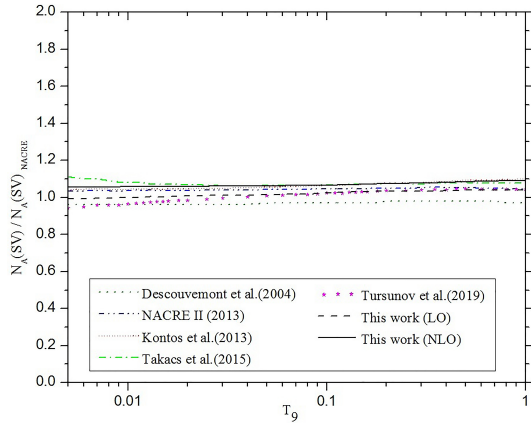


Fig. 6 The reaction rate of ${}^3\text{He}(\alpha, \gamma){}^7\text{Be}$ in the $10^6\text{K} \leq T \leq 10^9\text{K}$ ($0.001 \leq T_9 \leq 1$) temperature range in LO (dashed line) and NLO (solid line), normalized to the NACRE 1999 experimental data, was compared with other theoretical and experimental data.

thermonuclear reaction rate of the ${}^3\text{He}(\alpha, \gamma){}^7\text{Be}$ process up to NLO in this study. Table 1 contains the calculated values. In Fig.5, we compared our results in LO and NLO to the data of Kontos, A. et al. (2013); Takacs, M.P. et al. (2015); Tursunov, E.M. et al. (2019); Xua, Y. et al. (2013); Descouvemont, P. et al. (2004) as a function of temperature in the range of $0.001 \leq T_9 \leq 1$, where T_9 is the stellar temperature in GK . These results are also shown in Fig. 6 normalized to the Angulo, C. et al. (1999) (NACRE) experimental data.

At low temperatures, there is considerable variability in the reaction rate predictions, as shown in Table 1, due to the Coulomb repulsion between alpha and ${}^3\text{He}$ charged particles with identical charges. The presence of the Coulomb barrier, as we know, reduces the chance of collision and reaction speed at temperatures far lower than the Big Bang temperature, $T \sim 10T_9$.

This is also seen in Fig.5. The reaction rate is depicted in terms of T_9 in LO and NLO, along with various theoretical and experimental works, which demonstrate that at low temperatures, the reaction rate is substantially lower than the values associated with Big Bang temperatures. Furthermore, the results of our computations in Table 1 and Fig. 6 demonstrate a 4 to 6.5% improvement in NLO compared to LO calculation. At temperature $T_9 = 0.5$, for example, the NLO contribution is ~ 0.0324 , while the LO contribution is ~ 0.7346 , the total of which equals the NLO contribution ~ 0.7670 . The effects of Coulomb corrections are also taken into account in these computations, with a contribution of around 4%.

The normalized findings in Fig. 6 reveal that most theoretical and experimental studies are linear in the same temperature range. This is evident in our estimates in both LO and NLO. However, in NLO, the current computations show the best agreement with the Kontos, A. et al. (2013) and Takacs, M.P. et al. (2015) data when compared to other efforts, particularly in the temperature range of $0.02 \leq T_9 \leq 0.2$. Current estimates inside the EFT technique in NLO reveal an inaccuracy of roughly 0.6% in comparison to the rate of Kontos, A. et al. (2013) by the way of doing the R-matrix analysis for capturing reaction data at higher temperatures associated with BBN.

4 Summary and conclusions

${}^3\text{He}(\alpha, \gamma){}^7\text{Be}$ reaction has a dual role in astrophysics, estimating the abundance of primordial ${}^7\text{Li}$ and studying the solar neutrinos. Knowing the reaction rate in astrophysical energies is essential to understanding the abundance of elements in the Universe. In this work, the ${}^3\text{He}(\alpha, \gamma){}^7\text{Be}$ reaction rate has been computed within the pionless EFT procedure applying the Faddeev equation for the E_1 and E_2 transitions to the ${}^7\text{Be}$ ground state considering the Coulomb interaction. The findings in LO and NLO, as well as various experimental and theoretical investigations, are summarized in table 1, plotted in Fig.5, and displayed in Fig.6 after normalizing to the data of Angulo, C. et al. (1999). We found that the Coulomb contribution can modify the findings by roughly 4%, and the next-to-leading order computations enhanced the leading order data by (4 – 6.5)%. When compared to previous research, the experimental data agrees well, notably in the temperature range of $0.02 \leq T_9 \leq 0.2$.

Statements and declarations

- **Data Availability:** All data generated or analysed during this study are included in this published article.
- **Author Contribution:** B.C. conceived of the presented idea. B.C. developed the theory and performed the computations. A.B and A.C. verified the analytical methods. B.C. supervised the findings of this work. All authors discussed the results and contributed to the final manuscript.
- **Conflict of Interest:** Authors state no conflict of interest.
- **Funding:** No funding was received to assist with the preparation of this manuscript.

Table 1 Theoretical estimation of the reaction rates for the ${}^3\text{He}(\alpha, \gamma){}^7\text{Be}$ reaction in the temperature range of $10^6 K \leq T \leq 10^9 K$ ($0.001 \leq T_9 \leq 1$).

T_9	$N_A(\sigma\nu)_{[11]}$	$N_A(\sigma\nu)_{[12]}$	$N_A(\sigma\nu)_{[23]}$	$N_A(\sigma\nu)_{[8]}$	$N_A(\sigma\nu)_{[29]}$	$N_A(\sigma\nu)_{EFT(LO)}$	$N_A(\sigma\nu)_{EFT(NLO)}$
0.005	5.140×10^{-25}	5.185×10^{-25}	5.518×10^{-25}	4.766×10^{-25}	4.682×10^{-25}	4.929×10^{-25}	5.250×10^{-25}
0.006	3.790×10^{-23}	3.826×10^{-23}	4.040×10^{-23}	3.516×10^{-23}	3.478×10^{-23}	3.626×10^{-23}	3.859×10^{-23}
0.007	1.170×10^{-21}	1.184×10^{-21}	1.243×10^{-21}	1.088×10^{-21}	1.082×10^{-21}	1.124×10^{-21}	1.194×10^{-21}
0.008	1.990×10^{-20}	2.007×10^{-20}	2.096×10^{-20}	1.843×10^{-20}	1.842×10^{-20}	1.915×10^{-20}	2.030×10^{-20}
0.009	2.170×10^{-19}	2.191×10^{-19}	2.279×10^{-19}	2.012×10^{-19}	2.019×10^{-19}	2.094×10^{-19}	2.220×10^{-19}
0.010	1.700×10^{-18}	1.715×10^{-18}	1.778×10^{-18}	1.575×10^{-18}	1.585×10^{-18}	1.639×10^{-18}	1.735×10^{-18}
0.011	1.030×10^{-17}	1.035×10^{-17}	1.071×10^{-17}	9.506×10^{-18}	9.594×10^{-18}	9.88×10^{-18}	1.047×10^{-17}
0.012	5.030×10^{-17}	5.079×10^{-17}	5.240×10^{-17}	4.663×10^{-17}	4.718×10^{-17}	4.851×10^{-17}	5.133×10^{-17}
0.013	2.090×10^{-16}	2.104×10^{-16}	2.166×10^{-16}	1.932×10^{-16}	1.959×10^{-16}	2.020×10^{-16}	2.128×10^{-16}
0.014	7.510×10^{-16}	7.578×10^{-16}	7.789×10^{-16}	6.955×10^{-16}	7.068×10^{-16}	7.250×10^{-16}	7.660×10^{-16}
0.015	2.400×10^{-15}	2.426×10^{-15}	2.490×10^{-15}	2.227×10^{-15}	2.267×10^{-15}	2.328×10^{-15}	2.456×10^{-15}
0.016	6.960×10^{-15}	7.028×10^{-15}	7.203×10^{-15}	6.449×10^{-15}	6.577×10^{-15}	6.743×10^{-15}	7.108×10^{-15}
0.018	4.560×10^{-14}	4.609×10^{-14}	4.712×10^{-14}	4.228×10^{-14}	4.325×10^{-14}	4.429×10^{-14}	4.660×10^{-14}
0.020	2.300×10^{-13}	2.325×10^{-13}	2.372×10^{-13}	2.132×10^{-13}	2.186×10^{-13}	2.241×10^{-13}	2.353×10^{-13}
0.025	5.860×10^{-12}	5.918×10^{-12}	6.018×10^{-12}	5.424×10^{-12}	5.591×10^{-12}	5.693×10^{-12}	5.978×10^{-12}
0.030	6.880×10^{-11}	6.951×10^{-11}	7.019×10^{-11}	6.368×10^{-11}	6.589×10^{-11}	6.687×10^{-11}	7.015×10^{-11}
0.040	2.460×10^{-9}	2.493×10^{-9}	2.515×10^{-9}	2.282×10^{-9}	2.374×10^{-9}	2.399×10^{-9}	2.517×10^{-9}
0.050	3.110×10^{-8}	3.151×10^{-8}	3.177×10^{-8}	2.881×10^{-8}	3.010×10^{-8}	3.022×10^{-8}	3.167×10^{-8}
0.060	2.140×10^{-7}	2.168×10^{-7}	2.184×10^{-7}	1.980×10^{-7}	2.075×10^{-7}	2.082×10^{-7}	2.180×10^{-7}
0.070	9.920×10^{-7}	1.007×10^{-6}	1.013×10^{-6}	9.188×10^{-7}	9.648×10^{-7}	9.660×10^{-7}	1.011×10^{-6}
0.080	3.500×10^{-6}	3.560×10^{-6}	3.581×10^{-6}	3.247×10^{-6}	3.416×10^{-6}	3.422×10^{-6}	3.576×10^{-6}
0.090	1.020×10^{-5}	1.033×10^{-5}	1.038×10^{-5}	9.411×10^{-6}	9.916×10^{-6}	9.920×10^{-6}	1.035×10^{-5}
0.100	2.530×10^{-5}	2.578×10^{-5}	2.589×10^{-5}	2.348×10^{-5}	2.477×10^{-5}	2.477×10^{-5}	2.579×10^{-5}
0.110	5.620×10^{-5}	5.726×10^{-5}	5.747×10^{-5}	5.211×10^{-5}	5.504×10^{-5}	5.508×10^{-5}	5.729×10^{-5}
0.120	1.140×10^{-4}	1.159×10^{-4}	1.162×10^{-4}	1.054×10^{-4}	1.114×10^{-4}	1.119×10^{-4}	1.164×10^{-4}
0.130	2.130×10^{-4}	2.173×10^{-4}	2.178×10^{-4}	1.975×10^{-4}	2.090×10^{-4}	2.088×10^{-4}	2.170×10^{-4}
0.140	3.750×10^{-4}	3.826×10^{-4}	3.832×10^{-4}	3.476×10^{-4}	3.680×10^{-4}	3.689×10^{-4}	3.830×10^{-4}
0.150	6.25×10^{-4}	6.392×10^{-4}	6.398×10^{-4}	5.803×10^{-4}	6.149×10^{-4}	6.150×10^{-4}	6.390×10^{-4}
0.160	9.980×10^{-4}	1.021×10^{-3}	1.021×10^{-3}	9.263×10^{-4}	9.822×10^{-4}	9.810×10^{-4}	1.020×10^{-3}
0.180	2.280×10^{-3}	2.333×10^{-3}	2.331×10^{-3}	2.114×10^{-3}	2.244×10^{-3}	2.240×10^{-3}	2.330×10^{-3}
0.200	4.620×10^{-3}	4.739×10^{-3}	4.731×10^{-3}	4.291×10^{-3}	4.559×10^{-3}	4.543×10^{-3}	4.730×10^{-3}
0.250	1.890×10^{-2}	1.945×10^{-2}	1.936×10^{-2}	1.757×10^{-2}	1.869×10^{-2}	1.858×10^{-2}	1.936×10^{-2}
0.300	5.490×10^{-2}	5.655×10^{-2}	5.619×10^{-2}	5.097×10^{-2}	5.431×10^{-2}	5.398×10^{-2}	5.620×10^{-2}
0.350	1.280×10^{-1}	1.317×10^{-1}	1.306×10^{-1}	1.185×10^{-1}	1.264×10^{-1}	1.250×10^{-1}	1.304×10^{-1}
0.400	2.540×10^{-1}	2.635×10^{-1}	2.606×10^{-1}	2.364×10^{-1}	2.523×10^{-1}	2.510×10^{-1}	2.618×10^{-1}
0.450	4.540×10^{-1}	4.705×10^{-1}	4.652×10^{-1}	4.219×10^{-1}	4.504×10^{-1}	4.463×10^{-1}	4.660×10^{-1}
0.500	7.440×10^{-1}	7.731×10^{-1}	7.636×10^{-1}	6.923×10^{-1}	7.395×10^{-1}	7.346×10^{-1}	7.670×10^{-1}
0.600	1.670×10^0	1.739×10^0	1.714×10^0	1.553×10^0	1.660×10^0	1.653×10^0	1.728×10^0
0.700	3.160×10^0	3.296×10^0	3.243×10^0	2.935×10^0	3.140×10^0	3.132×10^0	3.277×10^0
0.800	5.300×10^0	5.550×10^0	5.454×10^0	4.932×10^0	5.278×10^0	5.267×10^0	5.515×10^0
0.900	8.170×10^0	8.582×10^0	8.422×10^0	7.608×10^0	8.145×10^0	8.115×10^0	8.513×10^0
1.000	1.180×10^1	1.245×10^1	1.220×10^1	1.101×10^1	1.179×10^1	1.173×10^1	1.231×10^1

References

- Angulo, C. et al.: Nuclear Physics A **656**, 3-183 (1999)
- Nara Singh, B. S. et al.: Phys. Rev. Lett. **93**, 262503 (2004)
- Confortola, F. et al.: Phys. Rev. c. **75**, 065803 (2007)
- Brown, T. A. D. et al.: Phys. Rev. C. **76**, 055801 (2007)
- Cyburt, R. H. et al.: Phys. Rev. C. **78**, 064614 (2008)
- Canton, L. et al.: Nucl. Phys. A. **808**, 192 (2008)
- Di Leva, A. et al.: Phys. Rev. Lett. **102**, 232502 (2009)
- Descouvemont, P. et al.: Atomic Data and Nuclear Data Tables **88**, 203 (2004)
- Neff, T.: Nucl.Phys. A. **66**, 341 (2010)
- Neff, T.: Phys. Rev. Lett. **106**, 042502 (2011)
- Xua, Y. et al.: Nuclear Physics A **918**, 61-169 (2013)
- Kontos, A. et al.: PHYSICAL REVIEW C **87**, 065804 (2013)
- Sadeghi, H. et al.: Chinese Physics C. **37**, 044102 (2013)
- Sadeghi, H. et al.: Astronomy and Astrophysics. **14**, 357 (2014a)
- Sadeghi, H. et al.: Astrophys. Space Sci. **352**, 637 (2014b)
- Zhang, X. et al.: J. Phys. G **47**, 054002 (2020)
- Premarathna, P. et al.: Eur. Phys. J. A **56**, 166 (2020)
- Higa, R. et al.: European Physical Journal A. **54**, 89 (2018)
- Nahidinezhad, S. et al.: New Astronomy. **80**, 101424 (2020a)
- Nahidinezhad, S. et al.: Astrophysics and Space Science. **4**, 365 (2020b)
- Nahidinezhad, S. et al.: New Astronomy. **82**, 101461 (2021)
- Nahidinezhad, S. et al.: New Astron. **91**, 101700 (2022)
- Takacs, M.P. et al.: Phys. Rev. D **91**, 123526 (2015)
- Nollett, K.M. et al.: Phys.Rev. D **61**, 123505 (2000)
- deBoer, R. J. et al.: Phys. Rev. C **90**, 035804 (2014)
- Sadeghi, H. et al.: Research in Astronomy and Astrophysics **14**, 367 (2013)
- Sadeghi, H. et al.: New Astronomy. **61**, 14 (2018)
- Iliadis, C. et al.: Astrophysical Journal **831**, 107 (2016)
- Tursunov, E.M. et al.: International Journal of Modern Physics: Conference Series **49**, 1960014 (2019)
- Khoddam. M. et al.: Astrophysics and space science **367**, 23 (2022a)
- Khoddam. M. et al.: Astroparticle physics (under consideration) , (2022b)
- Ji, C. et al.: Phys. Rev. C. **90**, 044004 (2014)